

Transforming Li_3PS_4 Via Halide Incorporation: a Path to Improved Ionic Conductivity and Stability in All-Solid-State Batteries

Tej P. Poudel, Michael J. Deck, Pengbo Wang, and Yan-Yan Hu*

To enhance Li^+ transport in all-solid-state batteries (ASSBs), harnessing localized nanoscale disorder can be instrumental, especially in sulfide-based solid electrolytes (SEs). In this investigation, the transformation of the model SE, Li_3PS_4 , is delved into via the introduction of LiBr . ^{31}P nuclear magnetic resonance (NMR) unveils the emergence of a glassy PS_4^{3-} network interspersed with Br^- . ^6Li NMR corroborates swift Li^+ migration between PS_4^{3-} and Br^- , with increased Li^+ mobility indicated by NMR relaxation measurements. A more than fourfold enhancement in ionic conductivity is observed upon LiBr incorporation into Li_3PS_4 . Moreover, a notable decrease in activation energy underscores the pivotal role of Br^- incorporation within the anionic lattice, effectively reducing the energy barrier for ion conduction and transitioning Li^+ transport dimensionality from 2D to 3D. The compatibility of Li_3PS_4 with Li metal is improved through LiBr incorporation, alongside an increase in critical current density from 0.34 to 0.50 mA cm^{-2} , while preserving the electrochemical stability window. ASSBs with $3\text{Li}_3\text{PS}_4:\text{LiBr}$ as the SE showcase robust high-rate and long-term cycling performance. These findings collectively indicate the potential of lithium halide incorporation as a promising avenue to enhance the ionic conductivity and stability of SEs.

applications from consumer electronics to electric vehicles to renewable energy storage, and enabled the development of new technologies. However, the use of flammable organic solvents in the current generation of LIBs often leads to safety hazards resulting from dendrite formation and thermal runaway.^[2] In addition, these liquid electrolytes are not typically compatible with Li-metal anodes.^[3] To mitigate safety hazards and increase energy densities, high-performance all-solid-state batteries (ASSBs) hold a promising future in energy storage by overcoming the current challenges of LIBs.^[3,4] The advancement of ASSBs is intricately linked to the progress in developing solid electrolytes (SEs). The use of SEs allows for the possible use of a metallic lithium anode,^[3,5] wide temperature operational range,^[6–10] and enhanced safety.^[11–13] The following properties are favorable in the development of superionic conductors as electrolytes in ASSBs: (1) ionic conductivity $> 1 \text{ mS cm}^{-1}$ with low activation energy,

(2) compatibility with electrodes over a wide electrochemical window, (3) low electronic conductivity, (4) chemical, mechanical, and thermal stability, (5) facile processing, (6) scalability, and (7) sustainability.^[14]

Various types of SEs are being developed, such as inorganic, polymer, and inorganic-polymer composite electrolytes.^[15] Inorganic lithium SEs can be categorized into sulfide, oxide, and halide SEs, each with advantages and disadvantages. Sulfide SEs hold great promise due to their ionic conductivity being comparable to that of liquid electrolytes ($\geq 10 \text{ mS cm}^{-1}$).^[16] However, their suitability is compromised by insufficient stability when paired with Li metal anodes and current commercial cathodes. Glass-ceramic composite electrolytes are gaining interest due to their high ionic conductivity, facile synthesis, and improved mechanical properties.^[8] Among the glass-ceramic SEs, $\beta\text{-Li}_3\text{PS}_4$ has attracted special attention due to its stability against Li. However, it exhibits low ionic conductivity on the order of $10^{-4} \text{ S cm}^{-1}$.^[17–19] Improvements in the conductivity of Li_3PS_4 have been achieved via the introduction of local disorder on the atomic^[16,20,21] as well as nanoscale by producing Li_3PS_4 -composite SEs.^[8,9,22,23]

Recent studies have shown that halogen anion incorporation into thiophosphate electrolytes can significantly increase Li^+

1. Introduction

Rechargeable lithium-ion batteries (LIBs) represent a revolutionary technological advancement, attributed to their characteristics such as high energy and power density, long cycle life, and versatility.^[1] LIBs have found widespread use in various

T. P. Poudel, M. J. Deck, P. Wang, Y.-Y. Hu
Department of Chemistry and Biochemistry
Florida State University
95 Chieftan Way, Tallahassee, FL 32306, USA
E-mail: yhu@fsu.edu

T. P. Poudel, Y.-Y. Hu
Materials Science and Engineering Program
Florida State University
2005 Levy Ave., Tallahassee, FL 32310, USA

Y.-Y. Hu
Center of Interdisciplinary Magnetic Resonance
National High Magnetic Field Laboratory
1800 East Paul Dirac Drive, Tallahassee, FL 32310, USA

The ORCID identification number(s) for the author(s) of this article can be found under <https://doi.org/10.1002/adfm.202309656>

DOI: 10.1002/adfm.202309656

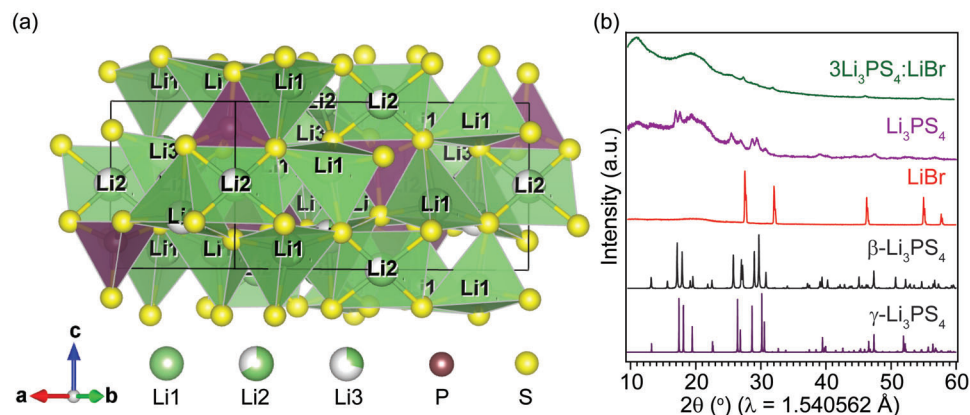


Figure 1. a) Crystal structure of β - Li_3PS_4 (ICSD #180319). b) PXRD patterns of Li_3PS_4 , LiBr , and $3\text{Li}_3\text{PS}_4:\text{LiBr}$. The XRD patterns of β - Li_3PS_4 (ICSD #180319) and γ - Li_3PS_4 (ICSD #180318) are shown as a reference. Broad Kapton film background at $\approx 20^\circ$.

conductivity and improve chemical stability.^[16,24–26] For example, reports on Li_3PS_4 with 30 mol% LiI have shown an increase in ionic conductivity along with an increase in critical current density (CCD).^[23,25,27] Furthermore, long-term mechanochemical milling of Li_3PS_4 with LiBr followed by ampule sintering was reported to increase the conductivity and air stability of Li_3PS_4 .^[28] However, more in-depth structural and electrochemical characterizations are needed to better understand the structure-property relation in Li_3PS_4 - LiX materials.

In this project, Li_3PS_4 and Li_3PS_4 - LiBr composite SEs are prepared via the solid-state mechanochemical milling method. The local structural environments of SEs are characterized using solid-state NMR and variable-temperature electrochemical impedance spectroscopy (EIS) is utilized to study Li^+ transport. With the incorporation of LiBr in Li_3PS_4 , a significant increase in ionic conductivity, critical current density (CCD), and compatibility against Li metal is obtained with no significant change in the electrochemical stability window. Galvanostatic cycling of solid-state half-cells using TiS_2 as the cathode active material (CAM) delivers improved cyclability of cells with LiBr -modified Li_3PS_4 compared to pristine Li_3PS_4 . This work provides an in-depth fundamental understanding of changes in the local structures and Li^+ dynamics upon LiBr incorporation into Li_3PS_4 and demonstrates its viability in ASSBs.

2. Results and Discussion

2.1. Structure

The synthesis process of Li_3PS_4 - LiBr is shown in the schematic diagram Figure S1 (Supporting Information) and uses a solid-state synthesis method (see the Supporting Information). Li_3PS_4 SEs were prepared with various hours (2.5–10 h) of ball milling time followed by powder sintering at 210°C for 2 h. Li_3PS_4 - LiBr SEs were then prepared by ball-milling the corresponding Li_3PS_4 with LiBr in 3:1 molar ratio for 2.5 h. Li_3PS_4 can crystallize in the γ -phase, which has relatively low Li^+ conductivity, or into the β -phase (Figure 1b), which has higher Li^+ conductivity.^[8] The phase transition to β -phase is reported at a temperature higher than 190°C for Li_3PS_4 , which is further aided by high-energy ball milling, which mimics quenching.^[8,29] The ionic conductiv-

ity of the β -phase is enhanced in comparison to the γ -phase by the emergence of octahedral sites for Li -ions migration due to the variation of the S^{2-} position into the zig-zag arrangement from the ordered arrangement in the γ -phase.^[29] The synthesized pristine compound, β - Li_3PS_4 , exhibits the $Pnma$ space group and is comprised of $(\text{PS}_4)^{3-}$ tetrahedral units with three different lithium sites, Li1 , Li2 , and Li3 (Figure 1a), corresponding to the 8d, 4b, and 4c Wyckoff positions, respectively. Bulk structure characterization of the samples was performed with powder X-ray diffraction (PXRD) and is shown in Figure 1b. Li_3PS_4 -BM-7.5 h and $3(\text{Li}_3\text{PS}_4\text{-BM-7.5 h}):\text{LiBr}$ are chosen as model systems for the reasons described below and denoted as Li_3PS_4 and $3\text{Li}_3\text{PS}_4:\text{LiBr}$ hereafter, respectively. The PXRD pattern of the Li_3PS_4 confirms the presence of a low crystalline (glassy) β - Li_3PS_4 phase.^[30] Whereas the PXRD pattern of composite samples is observed to be amorphous without any significant diffraction intensity, except the residual LiBr phase. The broad peak around 12° in the XRD of $3\text{Li}_3\text{PS}_4:\text{LiBr}$, is likely from the noncrystalline electrolyte phase, consistent with the broad resonance observed from ^{31}P NMR (Figure 2). Scanning electron microscopy (SEM) was utilized to examine the morphology of $3\text{Li}_3\text{PS}_4:\text{LiBr}$ and Li_3PS_4 and evaluate the impact of the second-stage ball milling step on grain size. Figure S2 (Supporting Information) shows that $3\text{Li}_3\text{PS}_4:\text{LiBr}$ and Li_3PS_4 exhibit a similar size distribution ranging from 0.5 to $2\ \mu\text{m}$. Moreover, because of the glass-ceramic nature of these thiophosphate SEs, solid-state NMR is necessary for accurate structural characterization due to its ability to probe the short- to medium-range structures.^[31]

To examine the effect of LiBr incorporation on local structural environments, ^6Li and ^{31}P MAS NMR experiments are performed.^[31] As shown in Figure 2a, the ^6Li signal of Li_3PS_4 resides at 0.9 ppm. A shoulder around 1.1 ppm is observed, accounting for 18% of the total Li amount and likely from γ -phase (quantification shown in Table S1 in the Supporting Information). After introducing LiBr into the Li_3PS_4 structural framework, the ^6Li signals shift to 0.5 ppm, indicating further changes to the Li environments. Solid LiBr has a ^6Li NMR shift of ≈ -1.9 ppm; Li^+ ions rapidly shuffling between $(\text{PS}_4)^{3-}$ and Br^- during transport will have an apparent shift between 0.9 and -1.9 ppm if the shuffling rate is much higher than the NMR time scale. The exact value depends on the relative ratio

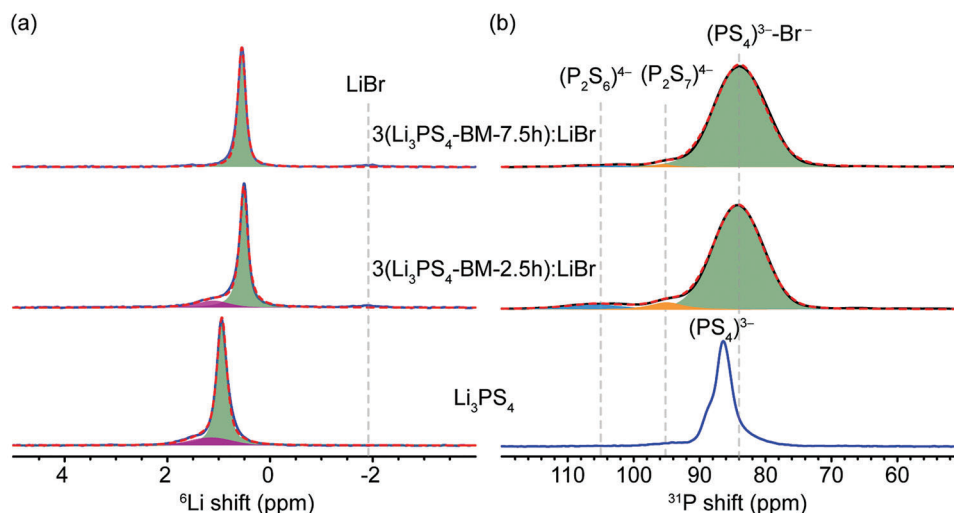


Figure 2. a) ${}^6\text{Li}$ and b) ${}^{31}\text{P}$ MAS NMR spectra of Li_3PS_4 , $3(\text{Li}_3\text{PS}_4\text{-BM-2.5 h})\text{:LiBr}$, and $3(\text{Li}_3\text{PS}_4\text{-BM-7.5 h})\text{:LiBr}$.

of $(\text{PS}_4)^{3-}$ and Br^- and the residential time of Li^+ on them. Meanwhile, both $\text{Li}_3\text{PS}_4\text{-LiBr}$ SEs with varying ball milling (BM) times of Li_3PS_4 , namely, $3(\text{Li}_3\text{PS}_4\text{-BM-7.5})\text{:LiBr}$ and $3(\text{Li}_3\text{PS}_4\text{-BM-2.5})\text{:LiBr}$, exhibit a narrower line shape than that of Li_3PS_4 , indicating increased Li^+ motion in the $3\text{Li}_3\text{PS}_4\text{-LiBr}$ SEs.^[32] The signal of the $3(\text{Li}_3\text{PS}_4\text{-BM-2.5})\text{:LiBr}$ sample shows a small peak around 1.4 ppm, attributed to the non-conductive $\text{Li}_4\text{P}_2\text{S}_6$.^[33] However, this peak is not present in the 7.5 h sample, implying a longer ball milling time for the preparation of the Li_3PS_4 can remove $\text{Li}_4\text{P}_2\text{S}_6$.

The incorporation of LiBr significantly changes the nature of the $(\text{PS}_4)^{3-}$ framework, as seen from the ${}^{31}\text{P}$ NMR (Figure 2b). Compared with Li_3PS_4 , the ${}^{31}\text{P}$ resonances of $\text{Li}_3\text{PS}_4\text{-LiBr}$ SEs become significantly broader and shift to lower ppm, which reflects the reduction of the crystallinity, echoing the results from PXRD and the introduction of Br^- . Li_3PS_4 begins with a major β - $(\text{PS}_4)^{3-}$ phase at 86 ppm and a minor γ - $(\text{PS}_4)^{3-}$ signal at around 88 ppm,^[34] while in $3(\text{Li}_3\text{PS}_4\text{-BM-7.5 h})\text{:LiBr}$ and $3(\text{Li}_3\text{PS}_4\text{-BM-2.5 h})\text{:LiBr}$ samples, the major resonance is from the glassy $(\text{PS}_4)^{3-}\text{-Br}^-$ unit around 84 ppm.^[35] In addition, two minor resonances at 95 ppm and 106 ppm are observed in $3(\text{Li}_3\text{PS}_4\text{-BM-2.5 h})\text{:LiBr}$, attributed to $(\text{P}_2\text{S}_7)^{4-}$ and $(\text{P}_2\text{S}_6)^{4-}$. $\text{Li}_4\text{P}_2\text{S}_6$ is a common and low-conducting impurity; the $3(\text{Li}_3\text{PS}_4\text{-BM-7.5 h})\text{:LiBr}$ shows no sign of $\text{Li}_4\text{P}_2\text{S}_6$.^[24] ${}^7\text{Li}$ NMR spin-lattice relaxation time (T_1) is a sensitive probe to Li^+ dynamics. Table 1 shows that $3(\text{Li}_3\text{PS}_4\text{-BM-7.5 h})\text{:LiBr}$ has a shorter T_1 than Li_3PS_4 , which indicates faster Li-ion motion.^[36,37] The slightly longer T_1 of $3(\text{Li}_3\text{PS}_4\text{-BM-2.5 h})\text{:LiBr}$ is an average value of the conductive phase and

Table 1. ${}^7\text{Li}$ spin-lattice relaxation time (T_1) of Li_3PS_4 , $3(\text{Li}_3\text{PS}_4\text{-BM-7.5 h})\text{:LiBr}$, and $3(\text{Li}_3\text{PS}_4\text{-BM-2.5 h})\text{:LiBr}$.

Sample	${}^7\text{Li } T_1$ [s]
Li_3PS_4	1.93
$3(\text{Li}_3\text{PS}_4\text{-BM-7.5 h})\text{:LiBr}$	1.72
$3(\text{Li}_3\text{PS}_4\text{-BM-2.5 h})\text{:LiBr}$	1.99

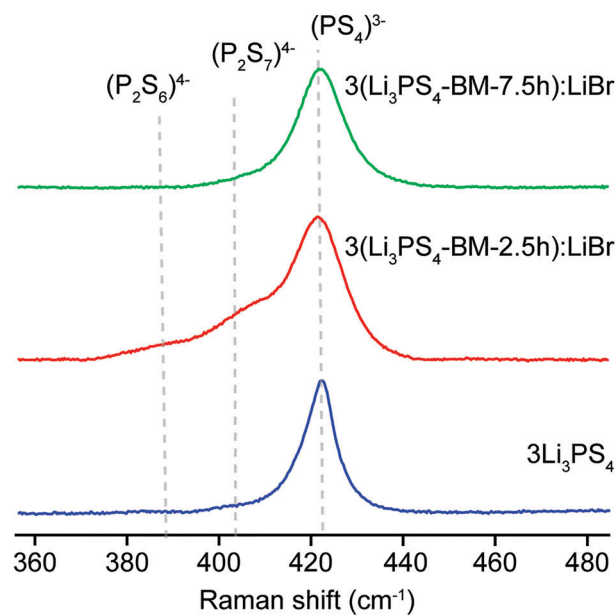


Figure 3. Raman spectra of Li_3PS_4 , $3(\text{Li}_3\text{PS}_4\text{-BM-7.5 h})\text{:LiBr}$, and $3(\text{Li}_3\text{PS}_4\text{-BM-2.5 h})\text{:LiBr}$.

nonconductive impurities as revealed in both ${}^7\text{Li}$ and ${}^{31}\text{P}$ NMR spectra.

Further characterization of the P-S bond nature is carried out using Raman spectroscopy. Raman spectroscopy is a short-range structural tool that can be used for determining thiophosphate polyhedrons, a useful complement to solid-state NMR. The Raman shift of the $(\text{PS}_4)^{3-}$ peak for all samples is observed at around 423 cm^{-1} .^[35] The presence of $(\text{P}_2\text{S}_7)^{4-}$ and low conducting $(\text{P}_2\text{S}_6)^{4-}$ impurities is observed for the sample with low overall ionic conductivity (Figure 3).^[38] The sample ball-milled for 7.5 h exhibits no signs of the impurity peaks.^[38] This is consistent with ${}^{31}\text{P}$ NMR results. The reduced amount of impurities is

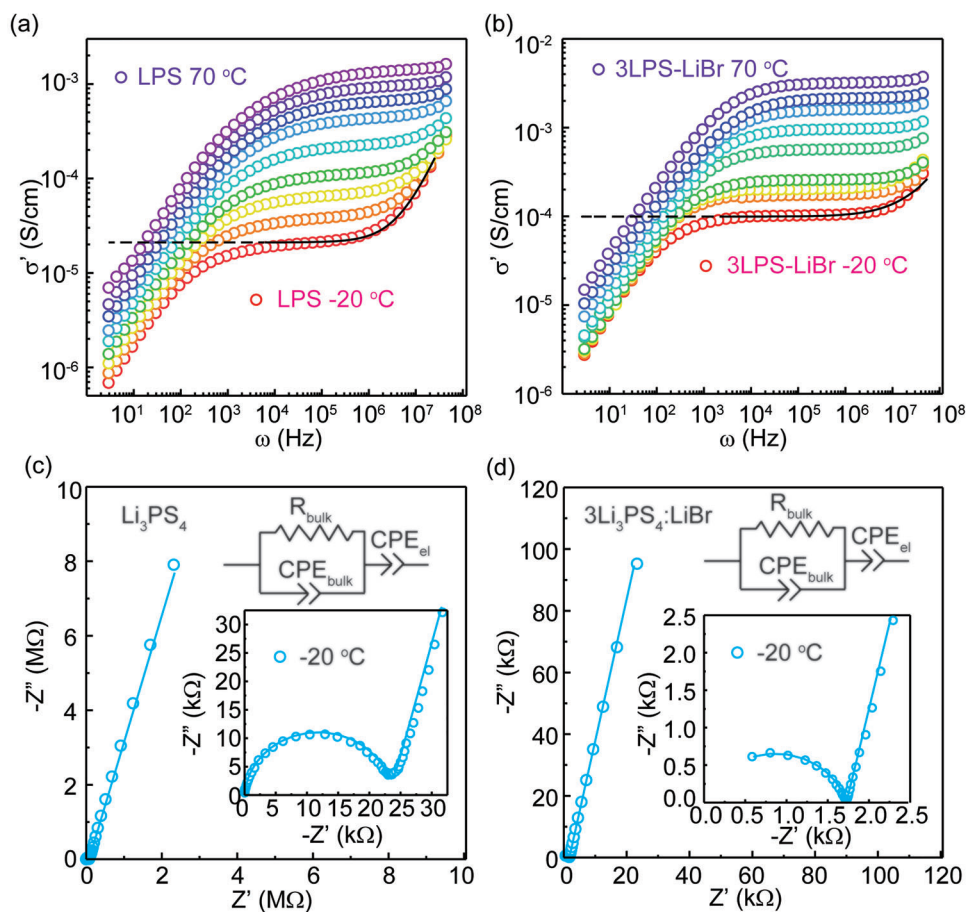


Figure 4. a,b) Conductivity isotherms and the Jonscher power law fitting for the isotherm at $-20\text{ }^{\circ}\text{C}$, for Li_3PS_4 and $3\text{Li}_3\text{PS}_4\text{:LiBr}$, respectively. c) Nyquist plot at $-20\text{ }^{\circ}\text{C}$ with equivalent circuit fitting (inset) for Li_3PS_4 . d) Nyquist plot at $-20\text{ }^{\circ}\text{C}$ with equivalent circuit fitting (inset) for $3\text{Li}_3\text{PS}_4\text{:LiBr}$.

likely responsible for the increase in conductivity (see below) for the longer ball-milled electrolyte, $3(\text{Li}_3\text{PS}_4\text{-BM-7.5 h})\text{:LiBr}$.

2.2. Fast-Ion Conduction in Li_3PS_4 with LiBr Incorporation

The electronic conductivity of $\text{Li}_3\text{PS}_4\text{-BM-7.5 h}$ and the corresponding $3\text{Li}_3\text{PS}_4\text{:LiBr}$ was measured by using the DC polarization method, as shown in Figure S3 in the Supporting Information. Very low electronic conductivities of $1.65 \times 10^{-9}\text{ S cm}^{-1}$ for Li_3PS_4 and $1.04 \times 10^{-9}\text{ S cm}^{-1}$ for $3\text{Li}_3\text{PS}_4\text{:LiBr}$ was measured at $25\text{ }^{\circ}\text{C}$. To investigate the effect of the introduction of LiBr on Li^+ transport, variable-temperature EIS measurements of the SEs were performed, and the representative $25\text{ }^{\circ}\text{C}$ Nyquist plots are shown in Figure S4 in the Supporting Information.

Variable-temperature EIS measurements were performed from -20 to $70\text{ }^{\circ}\text{C}$. From the conductivity isotherms, only one frequency-independent direct current (DC) plateau is observed (Figure 4a,b) which suggests the macroscopic Li^+ conduction involves the bulk process.^[39] To further confirm this, the equivalent circuit was fitted with the (RQ)Q type for the Nyquist plots at $-20\text{ }^{\circ}\text{C}$ (Figure 4c,d) and only one semicircle is detected, as expected, which confirms the macroscopic Li^+ conduction only

involves the bulk process. The conductivity was calculated from the equivalent circuit model fits using the following equation:

$$\sigma_{\text{DC}} = \frac{L}{R \times A} \quad (1)$$

where L and A are the thickness of the pellet and surface area of the blocking electrode, respectively, and R is the resistance extracted from the equivalent circuit fitting. For the $\text{Li}_2\text{S-P}_2\text{S}_5$ system, increasing the ball milling time increases the conductivity to 0.29 mS cm^{-1} for the sample milled for 10 h, compared with 0.16 mS cm^{-1} for the sample milled for 2.5 h. This increase in conductivity with longer ball milling time is likely associated with the higher reaction time between Li_2S and P_2S_5 , resulting in a $\beta\text{-Li}_3\text{PS}_4$ phase without impurity.^[8] With the incorporation of LiBr, a more than fourfold increase in conductivity is observed. The highest conductivity of 1.06 mS cm^{-1} is observed for the composite electrolyte with 7.5 h of ball-milling for the $\text{Li}_2\text{S-P}_2\text{S}_5$ system. These values align well with the trend from $^7\text{Li T}_1$ discussed above (Table 1). Figure 5a shows the room temperature ionic conductivity versus the $3\text{Li}_2\text{S:P}_2\text{S}_5$ (first stage) ball milling time, and Figure 5b shows the Arrhenius plot of the 7.5 h milled Li_3PS_4 and corresponding $3\text{Li}_3\text{PS}_4\text{:LiBr}$ SEs extracted from fitted Nyquist plots at variable temperatures. The Arrhenius-type

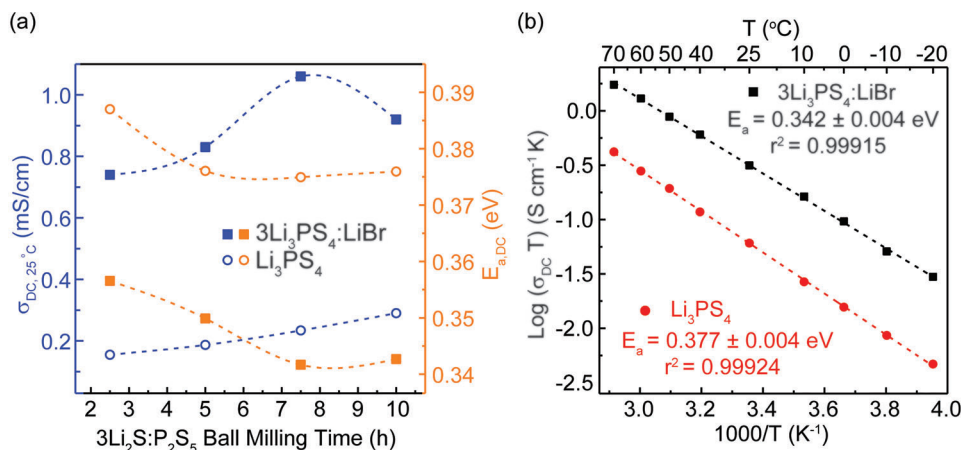


Figure 5. a) Effect of high-energy ball milling of 3Li₂S:P₂S₅ on the ionic conductivity and activation energy barriers of the final products: Li₃PS₄ and 3Li₃PS₄:LiBr (all the composite 3Li₃PS₄:LiBr were hand milled followed by high energy ball milling for 2.5 h). b) Arrhenius plots of ionic conductivity versus temperature ($1000/T$ (K⁻¹)) and the extracted activation energies (E_a) for ion transport in Li₃PS₄ and 3Li₃PS₄:LiBr synthesized with the optimal ball-milling time.

conductivity Equation (2) was used. The Arrhenius-type conductivity equation can be written as:

$$\sigma_{DC} T = \sigma_0 \exp^{-E_{a,DC}/k_B T} \quad (2)$$

where σ_{DC} is the DC ionic conductivity, T is the temperature in K, σ_0 is the Arrhenius prefactor, $E_{a,DC}$ is the activation energy, and k_B is the Boltzmann constant.^[40] From the Arrhenius relation (Equation 2), the conductivity increases with temperature. Arrhenius plots for all the prepared samples are shown in Figure S5 (Supporting Information) and Arrhenius prefactor (Figure S6 in the Supporting Information). EIS analysis result of all samples is listed in Table S2 in the Supporting Information. The $E_{a,DC}$ is calculated using the slope of the Arrhenius plots. The $E_{a,DC}$ of the β -Li₃PS₄ sample milled for 7.5 h is 0.38 eV, decreasing to 0.34 eV upon optimal LiBr incorporation, as shown in Figure 5a,b. The significant drop in activation energy with the incorporation of LiBr could be due to the increase in local disorder brought by LiBr incorporation in the Li₃PS₄ system.^[41] Local disorder via anion introduction distorts and creates a distribution of lithium site energies that allows for facile Li⁺ transfer from site to site, due to increased site energy overlap between neighboring Li-ions.^[42] Another potential reason for the increase in ionic conductivity can be a change in the dimensionality of Li⁺ transport from 2D to 3D, as has been predicted computationally upon optimal local disorder in Li₃PS₄^[43] as well as experimentally.^[44] To experimentally determine this, we further analyze the conductivity isotherms (Figure 4a,b) determined from VT-EIS and fit with the Jonscher power law, $\sigma' = \sigma_{DC} + A\omega^n$, where σ' is the AC conductivity, σ_{DC} is the DC ionic conductivity, A is the alternating current coefficient, and n is the power law exponent.^[44–46] n is an empirical indicator of the effective dimensions of ion conducting pathways for Li⁺ transport. A value of $n > 0.7$ indicates 3D conduction within the SE.^[47] The fitted n values are listed in Table 2. The value of n for Li₃PS₄ is 0.63, which indicates a 2D ion conductor and aligns well with that from the previous reports.^[47,48] Furthermore, an n value of 0.82 for 3Li₃PS₄:LiBr indicates 3D conduction. Therefore, with the incorporation of LiBr into Li₃PS₄,

the increase in ionic conductivity and decrease in activation energy is due to the local disorder that is introduced which leads to a “frustrated energy landscape” and prevents Li-ions from being energetically trapped.^[42,49,50]

2.3. Electrochemical Performance of Li₃PS₄ and 3Li₃PS₄:LiBr

With the observation of improved ionic conductivity for the SE upon LiBr incorporation, it is also important to examine the performance of the SE in battery cells.^[51] To understand the compatibility of the prepared SEs with Li metal, we performed critical current density (CCD) measurements on Li₃PS₄ and 3Li₃PS₄:LiBr SEs. The CCD against lithium metal is the maximum current density below which stable charge-discharge of ASSBs is possible.^[52] A high CCD of the SE is required for high-rate performance and is associated with the power density of the battery.^[53] The CCD is measured with Li/SE/Li symmetric cells as shown in Figure 6a,b. For the Li/Li₃PS₄/Li symmetric cell the CCD is 0.34 mA cm⁻², and the CCD increases to 0.50 mA cm⁻² for Li/3Li₃PS₄:LiBr/Li. The improvement in CCD for 3Li₃PS₄:LiBr is most likely due to the improved interfacial stability of the electrolyte with Li metal, increase in ionic conductivity, and decrease in electronic conductivity as shown in Figure S3 in the Supporting Information.^[51] The improved CCD indicates that 3Li₃PS₄:LiBr will facilitate fast charging of ASSBs in comparison to pristine Li₃PS₄.

Long-term cycling is performed at 0.1 mA cm⁻² for Li/SE/Li cells (Figure 6c). The Li/Li₃PS₄/Li symmetric cell fails after ≈ 6 days of cycling at room temperature; however, Li/3Li₃PS₄:LiBr/Li

Table 2. EIS analysis of Li₃PS₄ and 3Li₃PS₄:LiBr.

Sample	$\sigma_{DC,25^\circ C}$ [mS cm ⁻¹]	E_a [eV]	Log (σ_0) [S cm ⁻¹ K]	n
Li ₃ PS ₄	0.23	0.38	5.20	0.63
3Li ₃ PS ₄ :LiBr	1.06	0.34	5.22	0.82

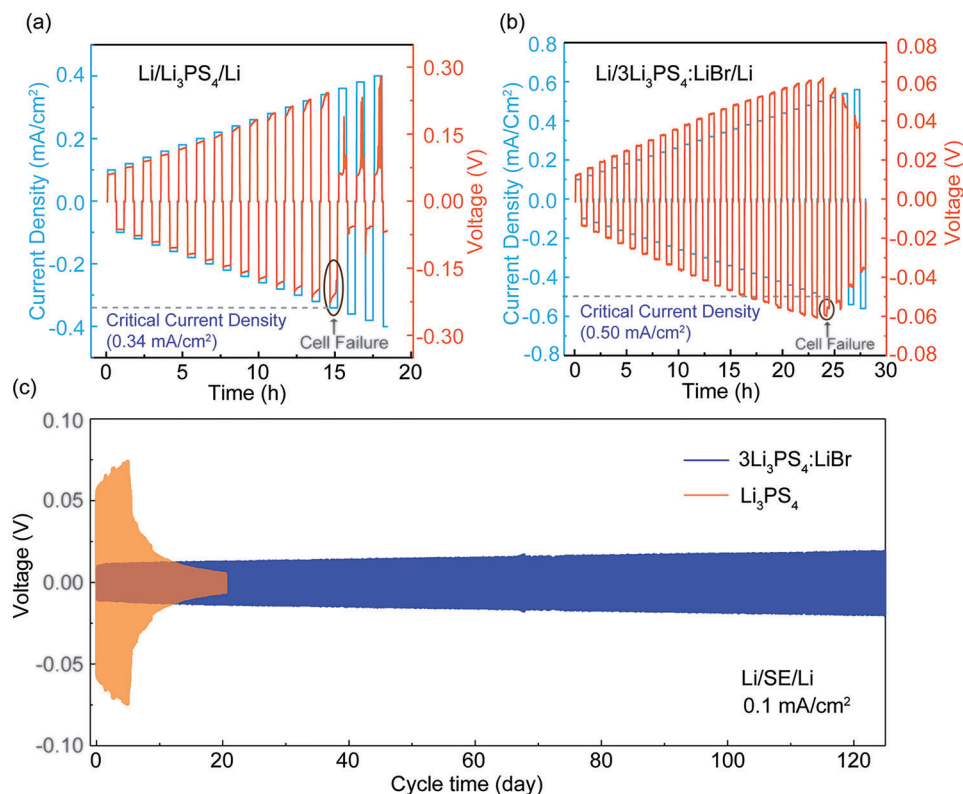


Figure 6. Electrochemical performance of $3\text{Li}_3\text{PS}_4\text{:LiBr}$ as solid electrolytes in $\text{Li}/\text{SE}/\text{Li}$ symmetric cells at 22°C , compared with Li_3PS_4 . a) Critical current density measurement of Li_3PS_4 , b) critical current density measurement of $3\text{Li}_3\text{PS}_4\text{:LiBr}$, c) long-term cycling performance of Li_3PS_4 and $3\text{Li}_3\text{PS}_4\text{:LiBr}$ at 0.1 mA cm^{-2} .

does not fail for over 125 days. The smaller increase in voltage over time for the $\text{Li}/3\text{Li}_3\text{PS}_4\text{:LiBr}/\text{Li}$ symmetric cell compared with the $\text{Li}/\text{Li}_3\text{PS}_4/\text{Li}$ cell (Figure 6c) indicates enhanced interfacial stability and improved compatibility of $3\text{Li}_3\text{PS}_4\text{:LiBr}$ with Li-metal.

Assessing the electrochemical stability window of the prepared high-conductive electrolytes and the pristine lithium thiophosphate is important for evaluating the electrochemical performance of the SE.^[54] The electrochemical potential window is the potential range in which the electrolytes and their components are not reactive and shows inertness towards the oxidation and reduction process.^{[55][56]} The traditional cyclic voltammetry (CV) measurement with stainless steel as the blocking electrode does not reflect the real voltage window of SEs and usually overestimates the potential window;^[54,57] accordingly the Li_3PS_4 and $3\text{Li}_3\text{PS}_4\text{:LiBr}$ CV cells were assembled using Li-In as the anode, SE separator, and a 3SE:C (mass ratio) composite cathode.^[58–62] Carbon is used here as an electronic conductive medium in a composite cathode which allows a more accurate measurement of degradation current due to its higher surface area and sensitive detection of degradation current.^[54,58–60,63] The stability window of Li_3PS_4 SEs was estimated computationally and found to be from 1.11 to 1.77 V versus Li-In.^[43,64]

Figure 7a shows the comparison of the cyclic voltammogram of Li_3PS_4 and $3\text{Li}_3\text{PS}_4\text{:LiBr}$ for the first two cycles. During the initial cycle, an onset of cathodic peak around $\approx 1.8\text{ V}$ versus Li-In is indicative of the probable formation of S_x^{2-} from S_x . This

may be attributed to the existence of unreacted sulfur within the electrolyte.^[41,60,65] Commencing from the second cycle onward, the sulfur reduction peak is no longer evident, as depicted in Figure S7 in the Supporting Information. $(\text{PS}_4)^{3-}$ oxidation (starting at $\approx 2.2\text{ V}$ vs Li-In) is prominent in the first anodic sweep and it decreases significantly for subsequent cycles (see Figure S7 in the Supporting Information), which can be attributed to the formation of passivation layers.^[54] The CV demonstrates the preservation of the stability window with LiBr incorporation, evidenced by the same redox and oxidation voltage onset of the peaks for both the cathodic and anodic sweep. $3\text{Li}_3\text{PS}_4\text{:LiBr}$ shows a smaller oxidation and reduction current than pristine Li_3PS_4 , indicating reduced oxidation and reduction reactions for $3\text{Li}_3\text{PS}_4\text{:LiBr}$, thus improved electrochemical stability.

Since the bulk SE is not at equilibrium during CV due to the fast scan rates used and has poor interfacial contact with the stainless steel current collector,^[61] we performed galvanostatic cycling of the carbon composite cells to further examine the stability^[60] and evaluate the intrinsic redox nature of sulfide SEs. The Li_3PS_4 and $3\text{Li}_3\text{PS}_4\text{:LiBr}$ carbon composite cells (identical to the one used for CV) were cycled galvanostatically and the corresponding capacities over 30 cycles are shown in Figure 7b with the voltage profile shown in Figure 7c,d. From the galvanostatic cycling results, we can observe capacity gain for both cells at $\approx 1.8\text{ V}$ for the 1st discharge due to the possible sulfur redox reaction (Figure 7c,d) also seen in the CV in Figure 7a. The voltage profile also aligns with the CV for the subsequent cycles; no

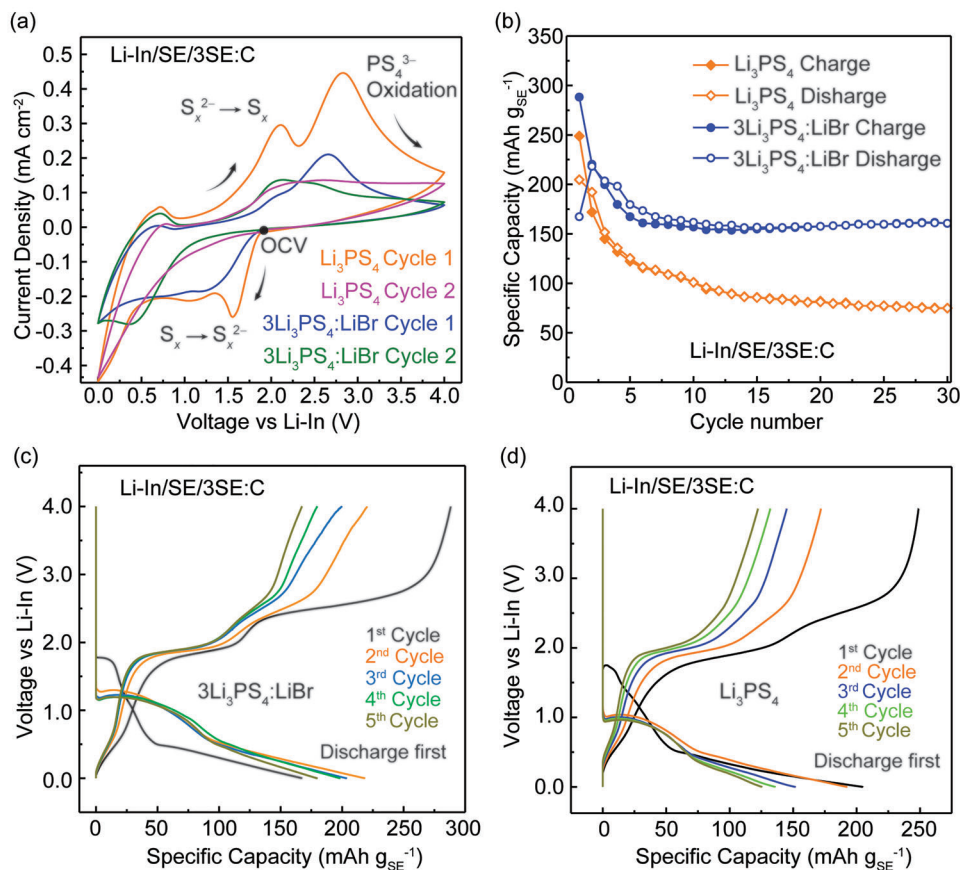


Figure 7. a) Cyclic voltammograms of Cycles 1 and 2 for Li_3PS_4 and $3\text{Li}_3\text{PS}_4:\text{LiBr}$ carbon-containing cells using a scan rate of 0.2 mV s^{-1} . See Figure S7 (Supporting Information) for voltammograms of Cycles 1–3. b) Room-temperature capacity versus cycle number for Li-In/SE/3SE:C . c) Selected voltage profiles of Cycles 1–5 of the $\text{Li-In/3Li}_3\text{PS}_4:\text{LiBr}/3(3\text{Li}_3\text{PS}_4:\text{LiBr}):C$ cell. d) Selected voltage profiles of Cycles 1–5 for $\text{Li-In/Li}_3\text{PS}_4/3\text{Li}_3\text{PS}_4:C$ cell. The current density used is 0.064 mA cm^{-2} .

capacity gain is observed at $\approx 1.8 \text{ V}$, which could be because the sulfur impurities are likely consumed due to redox reactions indicating that no reversible capacity is generated from the elemental sulfur $\rightarrow \text{Li}_2\text{S}$. The significant capacity gain at $\approx 1.0 \text{ V}$ versus Li-In after the first cycle can be attributed to the partially reversible SE lithiation/reduction^[43] which is also observed in the CV measurement. The cathodic peak at $\approx 0.6 \text{ V}$ versus Li-In can be assigned to the reduction (lithiation) of reversible redox product, P, to Li_3P .^[41,43,59] On the other hand the first peak in the anodic scan appears at $\approx 0.5 \text{ V}$ versus Li-In which can be assigned to the oxidation of reduced phosphorous species.^[41] The significant peak, located around $\approx 2 \text{ V}$ versus Li-In , is attributed to the oxidation process of decomposed components.^[55] This potentially indicates the reaction between Li_2S and Li_xP , leading to the creation of lithium thiophosphate glasses (including thiophosphate polyhedrons), a phenomenon observed in other thiophosphate SEs.^[41,54,58] This reaction is highly reversible and shows a stable cycling performance as shown in Figure 7c,d.^[54] A comparison of the differential capacity (Figure S8, Supporting Information) shows a similar redox behavior for both Li_3PS_4 and $3\text{Li}_3\text{PS}_4:\text{LiBr}$ SEs. The obtained stability window is ≈ 1.0 to 2.2 V versus Li-In for both Li_3PS_4 and $\text{Li}_3\text{PS}_4\text{-LiBr}$, which is larger than the computationally predicted limit ($1.11\text{--}1.77 \text{ V}$ vs Li-In).^[43]

Notable capacity is generated from SE redox and the redox products based on galvanostatic cycling of the 3SE:C composite cathode cell; this is beneficial if it occurs in the voltage window for ASSB operation and is reversible.^[58,59,66] The galvanostatic cycling of the Li_3PS_4 carbon-composite cell shows a higher first discharge capacity of $203 \text{ mAh g}_{\text{SE}}^{-1}$ than the $3\text{Li}_3\text{PS}_4:\text{LiBr}$ cell ($165 \text{ mAh g}_{\text{SE}}^{-1}$). However, the first charge capacity of the $3\text{Li}_3\text{PS}_4:\text{LiBr}$ carbon-composite cell is observed to be higher than that of the Li_3PS_4 carbon-composite cell. This could be because of the increase in ionic conductivity upon LiBr incorporation in Li_3PS_4 giving rise to a greater amount of the capacity-generating redox reactions that occur due to the improved reaction kinetics. Notably, for the initial cycle, PS_4^{3-} oxidation at high voltage contributes to additional capacity upon charge due to the formation of a passivation layer. For the 2nd cycle, $3\text{Li}_3\text{PS}_4:\text{LiBr}$ shows an increase in discharge capacity to $223 \text{ mAh g}_{\text{SE}}^{-1}$. The capacity increase could be caused by the redox activity of decomposed products created during the first cycle.^[58] During the 2nd charge, the capacity plateaus assigned to PS_4^{3-} oxidation decreases for both Li_3PS_4 and $3\text{Li}_3\text{PS}_4:\text{LiBr}$ cells from the passivation interphase formed, and the capacity decreases to $171 \text{ mAh g}_{\text{SE}}^{-1}$ and $220 \text{ mAh g}_{\text{SE}}^{-1}$ from $248 \text{ mAh g}_{\text{SE}}^{-1}$ and $288 \text{ mAh g}_{\text{SE}}^{-1}$, respectively. For both cells, part of the measured capacity below 1 V

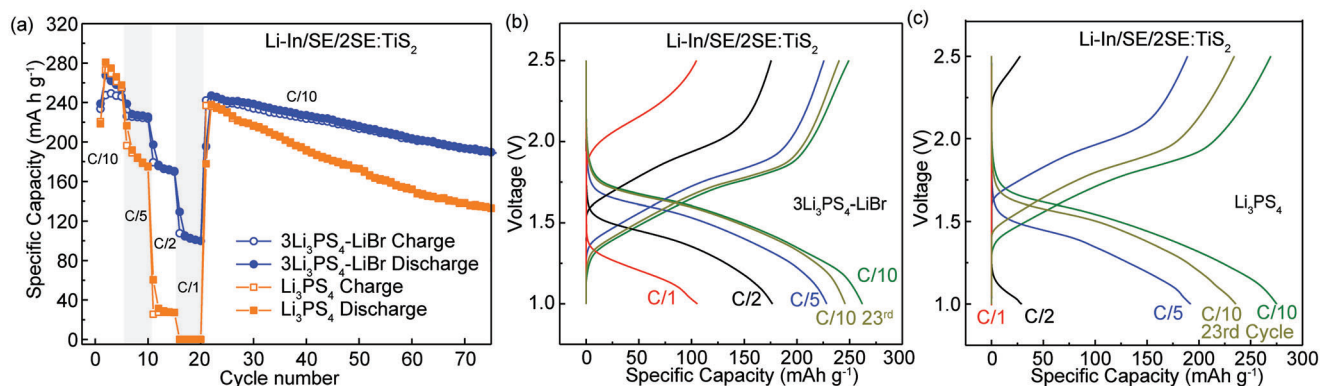


Figure 8. Rate performance cycling of Li-In/3Li₃PS₄:LiBr/2SE:TiS₂ and Li-In/Li₃PS₄/2SE:TiS₂ ASSB half-cells at charge discharge rates: C/10, C/5, C/2, and C/1. a) Capacity versus cycle number. b,c) Voltage profiles of the 2nd cycle at each C-rate for the ASSBs using 3Li₃PS₄:LiBr, and Li₃PS₄, respectively.

versus Li-In is partially attributed to Li intercalation into the Super P ($\approx 25 \text{ mAh g}^{-1}$).^[67] Figure 7b shows that Li₃PS₄ carbon-composite cells have almost half the capacity generated than 3Li₃PS₄:LiBr carbon-composite cells after 30 cycles.

To further investigate the electrochemical performance of the 3Li₃PS₄:LiBr electrolyte in ASSBs, half-cells containing Li₃PS₄ and 3Li₃PS₄:LiBr electrolytes were prepared using TiS₂ as the cathode active material (CAM) and Li-In alloy as the anode. From the Nyquist plots of half-cells at 22 °C and the equivalent circuit model shown in Figure S9 (Supporting Information), the bulk resistance of the SE and the CAM/SE resistance can be extracted (Table S3, Supporting Information).^[68] The CAM/SE resistance is of high importance as it can be indicative of chemical compatibility between the SE (Li₃PS₄ or Li₃PS₄:LiBr) and TiS₂, especially when compared between 2Li₃PS₄:TiS₂ and 2(3Li₃PS₄:LiBr):TiS₂. Accordingly, the CAM/SE resistance for 2Li₃PS₄:TiS₂ and 2(3Li₃PS₄:LiBr):TiS₂ is 100 and 191 Ω , respectively – indicating that upon Br introduction, the chemical compatibility of Li₃PS₄ with TiS₂ does not change significantly. The galvanostatic cycling was performed at various charge/discharge rates from 0.1 to 1 C (Figure 8a). A Li-In anode is used due to greater stability against SEs and less likely to creep through micropores to cause short circuits.^[69] The rate capabilities of the half-cells were measured at various charge–discharge rates (0.1 C $\approx 0.14 \text{ mA cm}^{-2}$, 0.2 C $\approx 0.28 \text{ mA cm}^{-2}$, 0.5 C $\approx 0.70 \text{ mA cm}^{-2}$, and 1 C $\approx 1.40 \text{ mA cm}^{-2}$) for 5 cycles followed by 35 cycles at 0.1 C using 239 mAh g⁻¹ as the theoretical capacity for TiS₂. The associated voltage profiles are shown in Figure 8b,c. The Li₃PS₄ cell shows a high initial capacity of around 280 mAh g⁻¹ for the 2nd cycle but exhibits 0 mAh g⁻¹ capacity at 1 C (Figure 8a,c). While the 3Li₃PS₄:LiBr cell is more stable and has a capacity of $\approx 117 \text{ mAh g}^{-1}$ for 1 C and the capacity fading is much slower compared to the Li₃PS₄ cell (Figure 8). The measured 1st cycle capacity for both half-cells is higher than the theoretical capacity of TiS₂ (239 mAh g⁻¹) which is likely due to the reversible SE redox,^[70] as observed in the same voltage range of the cycled SE-carbon composite cells, in addition to the unknown redox phases from reactions of the SE and TiS₂.^[71] Electronic conductivity measurements of the catholyte show the same trend as the pristine SEs, with the 3Li₃PS₄:LiBr containing catholyte having a smaller value than the Li₃PS₄ containing catholyte (Figure S10a, Supporting Information). PXRD peaks of the electroinactive TiS₂ remain

in both composites (Figure S10b, Supporting Information). The enhanced rate performance for the Li-In/3Li₃PS₄:LiBr /2SE:TiS₂ cell can be attributed to a convergence of the enhanced ionic conductivity, better stability of 3Li₃PS₄:LiBr versus Li metal, improved utilization of cathode active materials,^[72] and better redox reversibility of 3Li₃PS₄:LiBr than that of Li₃PS₄ (Figure 8b,c; Figure S11, Supporting Information).

3. Conclusion

With the incorporation of LiBr into β -Li₃PS₄, more than a four-fold increase in conductivity (0.23–1.06 mS cm⁻¹) is achieved resulting from the increased Li⁺ mobility, decreased activation energy barrier, and expanded dimensionality of Li⁺ transport paths from 2D to 3D. The comprehensive structural characterization using XRD (long-range), NMR (intermediate-/short-range), and Raman (short-range) unveils the loss of long-range structural order in 3Li₃PS₄:LiBr and the partition of Br⁻ within the PS₄³⁻ anion sublattice. Fast Li⁺ hopping between Br⁻ and (PS₄)³⁻ is implied by a single narrow Li NMR resonance. Furthermore, 3Li₃PS₄:LiBr demonstrates significantly improved critical current density and stability against Li metal. CV measurements show similar reversible redox characteristics for Li₃PS₄ and 3Li₃PS₄:LiBr, thus no significant change in the electrochemical stability window. 3Li₃PS₄:LiBr promotes high rate performance of ASSBs, retaining a specific capacity of 117 mAh g⁻¹ at 1 C for Li-In/3Li₃PS₄:LiBr/2SE:TiS₂, while the ASSB cell using Li₃PS₄ gives 0 mAh g⁻¹. Galvanostatic cell cycling reveals enhanced cyclability and electrochemical performance for long-term batteries using 3Li₃PS₄:LiBr, compared with Li₃PS₄. Enhanced ion transport via anion diversification can be applied to other Li₃PS₄-LiX (X = Cl, I) systems.^[16,49,73,74] A diversified anion sublattice prevents Li⁺ trapping, yielding increased ion mobility. In addition, the introduced local disorder often leads to a frustrated energy landscape, producing lower energy barriers for ion migration.

4. Experimental Section

Materials Synthesis: The Li₃PS₄-LiBr (3Li₃PS₄:LiBr) composite SE was prepared via the high-energy ball milling method. The schematic of the

synthesis process is shown in Figure S1 in the Supporting Information. The high-energy ball milling technique is leveraged for producing metastable materials that cannot be produced using the thermal equilibrium process.^[75] The two-stage ball milling was employed to synthesize the composite SE. A stoichiometric amount of Li_2S (99.98%, Sigma-Aldrich), and P_2S_5 (99%, Sigma-Aldrich) were mixed using mortar and pestle inside an argon-filled glovebox (Vacuum Technology). The solid mixture was then transferred into a zirconia milling jar and two zirconia balls (1 cm diameter) were added followed by vacuum sealing. The first stage of ball milling was carried out for various hours using an SPEX 8000 M high-energy miller. The prepared sample was then transferred to a sealed quartz tube inside an MBRAUN glovebox. The precursor powder was heated from room temperature to 210 °C at the ramping rate of 1 °C min⁻¹. The sintering temperature was chosen as 210 °C because the $\beta\text{-Li}_3\text{PS}_4$ phase forms at a temperature greater than 190 °C.^[8] The sample was heated for 2 h at 210 °C to synthesize the target $\beta\text{-Li}_3\text{PS}_4$.

To incorporate LiBr, as-prepared Li_3PS_4 was then mixed with LiBr at a 3:1 molar ratio in the glovebox using an agate mortar and pestle for 10 min to form a homogenous mixture. The mixture was then transferred into a zirconia milling jar with two zirconia balls of 1 cm diameter. The second stage high-energy ball milling was carried out for 2.5 h to produce $3\text{Li}_3\text{PS}_4\text{:LiBr}$ composite SEs. A 6-mm stainless-steel mold was then used to press 50 mg of powder sample at 300 MPa for 10 s to obtain a pellet of ≈ 1 mm thickness.

Materials Characterization: The sample for powder X-ray diffraction (PXRD) was prepared on a zero-background sample holder inside the glovebox to avoid the exposure of powder to oxygen and moisture. The powder was transferred to a sample holder, which was covered with Kapton film and sealed using vacuum grease. PXRD was carried out using Rigaku XtaLAB Synergy-S diffractometer with HyPix-6000He Hybrid Photon Counting detector using $\text{Cu K}\alpha$ ($\lambda = 1.5406 \text{ \AA}$) radiation. The PXRD of samples was performed at a scanning speed of 2.0° min⁻¹ within the 2θ range of 10°–60°.

Scanning electron microscope (SEM) images were obtained using a JEOL JSM-IT800 electron microscope (FE-SEM). ≈ 20 mg of sample powder was pressed in a 6 mm diameter stainless-steel mold at 300 MPa inside an argon-filled glovebox. The obtained pellet was then placed on the carbon tape in a vacuum-sealed sample holder. The sample holder was transferred into the exchange chamber of the JEOL JSM-IT800 and evacuated to ensure no air contamination on the pellets. An accelerating voltage of 5 kV was used and the SEM images were taken at the magnification of $\times 5.00 \text{ k}$ for the acquisition time of 1 min each.

Solid-state NMR experiments were carried out with an 11.75-T magnet and a 2.5-mm Bruker HXY probe. The samples were packed in 2.5-mm zirconia rotors and spun at the speed of 25 kHz. The ^6Li and ^7Li NMR spectra were obtained with single-pulse experiments with a flipping angle of 90°. The ^6Li and ^7Li shifts were referenced to solid LiCl at -1.1 ppm. $^7\text{Li T}_1$ was measured by using an inversion recovery pulse sequence. ^{31}P NMR spectra were collected using spin-echo experiments, and the ^{31}P shifts were referenced to 85% H_3PO_4 at 0 ppm. Raman spectra were collected using a Horiba JY LabRam HR Evolution Raman Spectrograph with a 633 nm excitation laser with a grating size of 1800 g mm⁻¹.

Impedance Measurements: The prepared pellet samples for both Li_3PS_4 and $3\text{Li}_3\text{PS}_4\text{:LiBr}$ series were sandwiched between two indium foils as blocking electrodes and assembled into an in-house built 6 mm dia cylindrical cell. Electrochemical impedance spectroscopy (EIS) was performed using a Gamry Reference 600+ in the frequency range of 0.1 Hz to 5 MHz. The bulk resistance was extracted from the Nyquist plot from EIS using an equivalent circuit model and the conductivity was calculated using Equation 1. Variable temperature EIS (VT-EIS) measurements were performed using a Biologic-SP300 in the CSZ microclimate chamber for heating and the activation energy was calculated using the Arrhenius-type equation.^[40]

DC Polarization: To measure the electronic conductivity, the DC polarization method was used.^[41] In-house built split cells (diameter = 10 mm) using PEEK insulating cylinder and stainless-steel plungers as current collectors and ion-blocking electrodes were used.

Symmetric-cell Cycling: In-house-built PEEK split cells with stainless-steel plungers as current collectors were utilized for both critical current density (CCD) and extended symmetric cycling. 120 mg of SE was pressed at 300 MPa, placed between 0.1 mm thick Li foil (1/4 inch diameter), and cycled at 5 MPa stack pressure.^[76] Cycling involved 30-min currents in alternating directions with 5-min breaks. In CCD tests, the used current density increased by 0.02 mA cm⁻² per cycle until cell shorting.

ASSB Assembly: The same PEEK split cells as described in the earlier section were employed for the assembly of ASSB half-cells. For cyclic voltammetry (CV) and galvanostatic cycling employing carbon-composite half-cells, initially, 100 mg of SE was pressed in the split cells at 300 MPa for 10 s. Subsequently, ≈ 12 mg of the manually mixed 3SE:Carbon black (carbon is Super P) composite was uniformly spread onto one surface of the pellet and pressed at 300 MPa for 10 s. On the other side of the pellet, a piece of In foil measuring 5/16 inch diameter and 0.1 mm thickness, weighing ≈ 32 mg was placed onto the pellet followed by Li foil with a diameter of 3/16 inch diameter and weighing ≈ 1 mg. The cell was sealed using vacuum grease and then cycled under ≈ 30 MPa stack pressure at 22 °C. For CV measurements, a scan rate of 0.2 mV s⁻¹ was used within a voltage range of 0–4 V versus Li-In. A current density of 0.064 mA cm⁻² was employed for the cells to cycle galvanostatically within the voltage window 0–4 V versus Li-In.

For $\text{TiS}_2\text{:2SE}$ half-cells, TiS_2 (Sigma, 99.9%) was first dried at 200 °C for 12 h to get rid of any adsorbed H_2O followed by planetary milling for 5 h at 300 RPM to decrease particle size.^[77] Subsequently, the composite cathode was then manually mixed with Li_3PS_4 or $3\text{Li}_3\text{PS}_4\text{:LiBr}$ in a 1:2 ($\text{TiS}_2\text{:SE}$) mass ratio using a mortar and pestle for 10 min. First, 100 mg of SE was pressed at 300 MPa for 10 s. Then, around 12 mg of catholyte was evenly distributed on one side of the pellet, corresponding to an aerial loading of ≈ 1.25 mAh cm⁻², and pressed at 300 MPa for 10 s. On the opposite side of the pellet, a piece of indium foil (with a diameter of 5/16 inches) weighing roughly 32 mg was placed followed by Li foil (with a diameter of 3/16 inches) weighing about 1 mg. After sealing with vacuum grease, cells were cycled under ≈ 30 MPa stack pressure at 22 °C between 1 and 2.5 V versus Li-In.

Supporting Information

Supporting Information is available from the Wiley Online Library or from the author.

Acknowledgements

The authors acknowledge the support from the National Science Foundation under grant no. DMR-1847038 and from the NSF MRSEC program (NSF DMR-1720139). All solid-state NMR experiments were performed at the National High Magnetic Field Laboratory, which is supported by National Science Foundation Cooperative Agreement Nos. DMR-1644779 and DMR-2128556*. The authors would like to thank William Stoffel for his help with the design of the in-house built split cells.

Conflict of Interest

The authors declare no conflict of interest.

Data Availability Statement

The data that support the findings of this study are available from the corresponding author upon reasonable request.

Keywords

batteries, energy storage, local disorder, solid electrolytes, solid-state NMR, stability

Received: August 14, 2023
Revised: October 8, 2023
Published online: October 20, 2023

- [1] Y. Sun, N. Liu, Y. Cui, *Nat. Energy* **2016**, *1*, 16071.
- [2] Y. Chen, Y. Kang, Y. Zhao, L. Wang, J. Liu, Y. Li, Z. Liang, X. He, X. Li, N. Tavajohi, B. Li, *J. Energy Chem.* **2021**, *59*, 83.
- [3] W. D. Richards, L. J. Miara, Y. Wang, J. C. Kim, G. Ceder, *Chem. Mater.* **2016**, *28*, 266.
- [4] N. Boaretto, I. Garbayo, S. Valiyaveetil-Sobhanraj, A. Quintela, C. Li, M. Casas-Cabanas, F. Aguesse, *J. Power Sources* **2021**, *502*, 229919.
- [5] H. Budde-Meiwes, J. Drillikens, B. Lunz, J. Muennix, S. Rothgang, J. Kowal, D. U. A. Sauer, *Proc. Inst. Mech. Eng. Part J. Automob. Eng.* **2013**, *227*, 761.
- [6] N. W. Nitta, F. Lee, J. T. Yushin, G. Li-Ion, *Mater. Today* **2015**, *18*, 252.
- [7] X. Li, J. Liang, X. Yang, K. R. Adair, C. Wang, F. Zhao, X. Sun, *Energy Environ. Sci.* **2020**, *13*, 1429.
- [8] Z. Liu, W. Fu, E. A. Payzant, X. Yu, Z. Wu, N. J. Dudney, J. Kiggans, K. Hong, A. J. Rondinone, C. Liang, *J. Am. Chem. Soc.* **2013**, *135*, 975.
- [9] S. Wang, Q. Bai, A. M. Nolan, Y. Liu, S. Gong, Q. Sun, Y. Mo, *Angew. Chem., Int. Ed. Engl.* **2019**, *58*, 8039.
- [10] R. Schlem, A. Banik, S. Ohno, E. Suard, W. G. Zeier, *Chem. Mater.* **2021**, *33*, 327.
- [11] Y. Guo, S. Wu, Y.-B. He, F. Kang, L. Chen, H. Li, Q.-H. Yang, *eScience* **2022**, *2*, 138.
- [12] H. Budde-Meiwes, J. Drillikens, B. Lunz, J. Muennix, S. Rothgang, J. Kowal, D. Sauer, *Proc. Inst. Mech. Eng. Part J. Automob. Eng.* **2013**, *227*, 761.
- [13] T. M. Gür, *Energy Environ. Sci.* **2018**, *11*, 2696.
- [14] J. C. Bachman, S. Mui, A. Grimaud, H.-H. Chang, N. Pour, S. F. Lux, O. Paschos, F. Maglia, S. Lupart, P. Lamp, L. Giordano, Y. Shao-Horn, *Chem. Rev.* **2016**, *116*, 140.
- [15] W. Zhao, J. Yi, P. He, H. Zhou, *Electrochem. Energy Rev.* **2019**, *2*, 574.
- [16] S. V. Patel, S. Banerjee, H. Liu, P. Wang, P.-H. Chien, X. Feng, J. Liu, S. P. Ong, Y.-Y. Hu, *Chem. Mater.* **2021**, *33*, 1435.
- [17] M. Tatsumisago, A. Hayashi, *Solid State Ion* **2012**, *225*, 342.
- [18] A. Sakuda, A. Hayashi, M. Tatsumisago, *Sci. Rep.* **2013**, *3*, 2261.
- [19] M. Suyama, A. Kato, A. Sakuda, A. Hayashi, M. Tatsumisago, *Electrochim. Acta* **2018**, *286*, 158.
- [20] K.-H. Kim, S. W. Martin, *Chem. Mater.* **2019**, *31*, 3984.
- [21] A. Neveu, V. Pelé, C. Jordy, V. Pralong, *J. Power Sources* **2020**, *467*, 228250.
- [22] T. Tsujimura, S. Ito, K. Yoshida, Y. Higashiyama, Y. Aihara, N. Machida, Y. Park, D. Im, *Solid State Ionics* **2022**, *383*, 115970.
- [23] E. Rangasamy, Z. Liu, M. Gobet, K. Pilar, G. Sahu, W. Zhou, H. Wu, S. Greenbaum, C. Liang, *J. Am. Chem. Soc.* **2015**, *137*, 1384.
- [24] P. Wang, H. Liu, S. Patel, X. Feng, P.-H. Chien, Y. Wang, Y.-Y. Hu, *Chem. Mater.* **2020**, *32*, 3833.
- [25] F. Han, J. Yue, X. Zhu, C. Wang, *Adv. Energy Mater.* **2018**, *8*, 1703644.
- [26] X. Feng, P.-H. Chien, Y. Wang, S. Patel, P. Wang, H. Liu, M. Immediato-Scuotto, Y.-Y. Hu, *Energy Storage Mater.* **2020**, *30*, 67.
- [27] P. Bonnick, K. Niitani, M. Nose, K. Suto, T. S. Arthur, J. Muldoon, *J. Mater. Chem. A* **2019**, *7*, 24173.
- [28] G. Wang, P. Dong, B. Liang, C. Lin, X. Shen, S. Dai, Q. Jiao, *J. Am. Ceram. Soc.* **2022**, *105*, 7751.
- [29] L. Pan, L. Zhang, A. Ye, S. Chi, Z. Zou, B. He, L. Chen, Q. Zhao, D. Wang, S. Shi, *J. Materiomics* **2019**, *5*, 688.
- [30] I. Levin, NIST Inorganic Crystal Structure Database (ICSD), **2020**, <https://doi.org/10.18434/M32147>.
- [31] X. Li, M. Deck, Y.-Y. Hu, in *Transition Metal Oxides for Electrochemical Energy Storage*, (Eds.: J. Nanda, V. Augustyn), John Wiley & Sons, Ltd, Hoboken, New Jersey, USA **2022**; pp. 299–318.
- [32] J. Gamon, M. S. Dyer, B. B. Duff, A. Vasilenko, L. M. Daniels, M. Zanella, M. W. Gaultois, F. Blanc, J. B. Claridge, M. J. Rosseinsky, *Chem. Mater.* **2021**, *33*, 8733.
- [33] H. Eckert, Z. Zhang, J. H. Kennedy, *Chem. Mater.* **1990**, *2*, 273.
- [34] M. Gobet, S. Greenbaum, G. Sahu, C. Liang, *Chem. Mater.* **2014**, *26*, 3558.
- [35] X. Chi, Y. Zhang, F. Hao, S. Kmiec, H. Dong, R. Xu, K. Zhao, Q. Ai, T. Terlier, L. Wang, L. Zhao, L. Guo, J. Lou, H. L. Xin, S. W. Martin, Y. Yao, *Nat. Commun.* **2022**, *13*, 2854.
- [36] J. Popovic, D. Brandell, S. Ohno, K. B. Hatzell, J. Zheng, Y.-Y. Hu, *J. Mater. Chem. A* **2021**, *9*, 6050.
- [37] N. Wu, P.-H. Chien, Y. Qian, Y. Li, H. Xu, N. S. Grundish, B. Xu, H. Jin, Y.-Y. Hu, G. Yu, J. B. Goodenough, *Angew. Chem.* **2020**, *132*, 4160.
- [38] A. Miura, N. C. Rosero-Navarro, A. Sakuda, K. Tadanaga, N. H. H. Phuc, A. Matsuda, N. Machida, A. Hayashi, M. Tatsumisago, *Nat. Rev. Chem.* **2019**, *3*, 189.
- [39] S. Lunghammer, Q. Ma, D. Rettenwander, I. Hanzu, F. Tietz, H. M. R. Wilkening, *Chem. Phys. Lett.* **2018**, *701*, 147.
- [40] Y. Gao, A. M. Nolan, P. Du, Y. Wu, C. Yang, Q. Chen, Y. Mo, S.-H. Bo, *Chem. Rev.* **2020**, *120*, 5954.
- [41] S. Ohno, C. Rosenbach, G. F. Dewald, J. Janek, W. G. Zeier, *Adv. Funct. Mater.* **2021**, *31*, 2010620.
- [42] Y. Zeng, B. Ouyang, J. Liu, Y.-W. Byeon, Z. Cai, L. J. Miara, Y. Wang, G. Ceder, *Science* **2022**, *378*, 1320.
- [43] S. Banerjee, M. L. Holekevi Chandrappa, S. P. Ong, *ACS Appl. Energy Mater.* **2022**, *5*, 35.
- [44] J. L. Ndeugueu, M. Aniya, *J. Phys. Soc. Jpn.* **2010**, *79*, 72.
- [45] I. Hanghofer, M. Brinek, S. L. Eisbacher, B. Bitschnau, M. Volck, V. Hennige, I. Hanzu, D. Rettenwander, H. M. R. Wilkening, *Phys. Chem. Chem. Phys.* **2019**, *21*, 8489.
- [46] O. Kamishima, Y. Iwai, J. Kawamura, *Solid State Ionics* **2015**, *281*, 89.
- [47] D. L. Sidebottom, *Rev. Mod. Phys.* **2009**, *81*, 999.
- [48] D. L. Sidebottom, *Phys. Rev. Lett.* **1999**, *83*, 983.
- [49] M. J. Deck, Y.-Y. Hu, *J. Mater. Res.* **2023**, *38*, 2631.
- [50] M. Botros, J. Janek, *Science* **2022**, *378*, 1273.
- [51] S. Sarkar, V. Thangadurai, *ACS Energy Lett.* **2022**, *7*, 1492.
- [52] F. Flatscher, M. Philipp, S. Ganschow, H. M. R. Wilkening, D. Rettenwander, *J. Mater. Chem. A* **2020**, *8*, 15782.
- [53] Y. Lu, C.-Z. Zhao, H. Yuan, X.-B. Cheng, J.-Q. Huang, Q. Zhang, *Adv. Funct. Mater.* **2021**, *31*, 2009925.
- [54] G. F. Dewald, S. Ohno, M. A. Kraft, R. Koerver, P. Till, N. M. Vargas-Barbosa, J. Janek, W. G. Zeier, *Chem. Mater.* **2019**, *31*, 8328.
- [55] P. Peljo, H. H. Girault, *Energy Environ. Sci.* **2018**, *11*, 2306.
- [56] Y. Zhu, X. He, Y. Mo, *ACS Appl. Mater. Interfaces* **2015**, *7*, 23685.
- [57] S. Wang, X. Wu, Y. Liang, Y. Xu, S. Guan, K. Wen, X. Miao, Y. Liang, H. He, Y. Lin, Y. Shen, C.-W. Nan, *Front. Chem. Eng.* **2022**, *4*.
- [58] D. H. S. Tan, E. A. Wu, H. Nguyen, Z. Chen, M. A. T. Marple, J.-M. Doux, X. Wang, H. Yang, A. Banerjee, Y. S. Meng, *ACS Energy Lett.* **2019**, *4*, 2418.
- [59] T. K. Schwietert, V. A. Arszewska, C. Wang, C. Yu, A. Vasileiadis, N. J. J. De Klerk, J. Hageman, T. Hupfer, I. Kerkamm, Y. Xu, E. Van Der Maas, E. M. Kelder, S. Ganapathy, M. Wagemaker, *Nat. Mater.* **2020**, *19*, 428.
- [60] Y. Tian, T. Shi, W. D. Richards, J. Li, J. C. Kim, S.-H. Bo, G. Ceder, *Energy Environ. Sci.* **2017**, *10*, 1150.
- [61] F. Han, Y. Zhu, X. He, Y. Mo, C. Wang, *Adv. Energy Mater.* **2016**, *6*, 1501590.
- [62] S. Wang, R. Fang, Y. Li, Y. Liu, C. Xin, F. H. Richter, C.-W. Nan, *J. Materiomics* **2021**, *7*, 209.

- [63] A. D. Bui, S.-H. Choi, H. Choi, Y.-J. Lee, C.-H. Doh, J.-W. Park, B. G. Kim, W.-J. Lee, S.-M. Lee, Y.-C. Ha, *ACS Appl. Energy Mater.* **2021**, *4*, 1.
- [64] T. Hakari, M. Deguchi, K. Mitsuhashi, T. Ohta, K. Saito, Y. Orikasa, Y. Uchimoto, Y. Kowada, A. Hayashi, M. Tatsumisago, *Chem. Mater.* **2017**, *29*, 4768.
- [65] K. Takada, M. Osada, N. Ohta, T. Inada, A. Kajiyama, H. Sasaki, S. Kondo, M. Watanabe, T. Sasaki, *Solid State Ionics* **2005**, *176*, 2355.
- [66] T. Hakari, M. Nagao, A. Hayashi, M. Tatsumisago, *J. Power Sources* **2015**, *293*, 721.
- [67] K. A. See, M. A. Lumley, G. D. Stucky, C. P. Grey, R. Seshadri, *J. Electrochem. Soc.* **2017**, *164*, A327.
- [68] W. Zhang, F. H. Richter, S. P. Culver, T. Leichtweiss, J. G. Lozano, C. Dietrich, P. G. Bruce, W. G. Zeier, J. Janek, *ACS Appl. Mater. Interfaces* **2018**, *10*, 22226.
- [69] J. Qu, J. Xiao, T. Wang, D. Legut, Q. Zhang, *J. Phys. Chem. C* **2020**, *124*, 24644.
- [70] D. Y. Oh, Y. E. Choi, D. H. Kim, Y.-G. Lee, B.-S. Kim, J. Park, H. Sohn, Y. S. Jung, *J. Mater. Chem. A* **2016**, *4*, 10329.
- [71] B. R. Shin, Y. J. Nam, J. W. Kim, Y.-G. Lee, Y. S. Jung, *Sci. Rep.* **2014**, *4*, 5572.
- [72] P. Minnmann, L. Quillman, S. Burkhardt, F. H. Richter, J. Janek, *J. Electrochem. Soc.* **2021**, *168*, 040537.
- [73] S. V. Patel, E. Truong, H. Liu, Y. Jin, B. L. Chen, Y. Wang, L. Miara, R. Kim, Y.-Y. Hu, *Energy Storage Mater.* **2022**, *51*, 88.
- [74] X. Feng, P.-H. Chien, Z. Zhu, I.-H. Chu, P. Wang, M. Immediato-Scuotto, H. Arabzadeh, S. P. Ong, Y.-Y. Hu, *Adv. Funct. Mater.* **2019**, *29*, 1807951.
- [75] D. L. Zhang, *Prog. Mater. Sci.* **2004**, *49*, 537.
- [76] J.-M. Doux, H. Nguyen, D. H. S. Tan, A. Banerjee, X. Wang, E. A. Wu, C. Jo, H. Yang, Y. S. Meng, *Adv. Energy Mater.* **2020**, *10*, 1903253.
- [77] J. E. Trevey, C. R. Stoldt, S.-H. Lee, *J. Electrochem. Soc.* **2011**, *158*, A1282.